Data report: characterization of iron oxides and iron sulfides in sediments from IODP Expedition 385 Sites U1549 and U1552 using rock magnetism and geochemistry[1]

Myriam Kars,[2, 3] Lucie Pastor,[2] Céline Burin,[4] and Louise M.T. Koornneef[2]

Contents

Abstract

Guaymas Basin is a young marginal rift basin in the Gulf of California, Mexico, characterized by active seafloor spreading and rapid sediment deposition, including organic-rich sediments. International Ocean Discovery Program (IODP) Expedition 385 drilled two sites near the Sonora margin, Sites U1549 and U1552, that are both close to a gas upflow pipe with Site U1549 being more distal to the corresponding upflow zone than Site U1552. Attenuated cold seepage conditions exist at Site U1549 in the central basin with methane occurrence below 25 meters below seafloor (mbsf), and hydrate was found to be present from ~25 mbsf at Site U1552. These two sites, ~12 km apart, represent an opportunity to study the influence of gas hydrate occurrence and methane seepage in shallow young organic-rich sediments (<170 mbsf; <0.29 Ma). In this data report, we present rock magnetic and geochemical data obtained from Sites U1549 and U1552 to characterize aqueous, solid iron, and sulfur phases present in the sediments, with a focus on iron oxides and iron sulfides. Guaymas Basin sediments are rich in reactive iron, mainly as pyrite. Iron oxides (magnetite and hematite) and authigenic iron sulfides (pyrite and greigite) are ubiquitously found in the sediments, and iron oxides are reduced to form pyrite. Pore water analysis seems to characterize current environmental and diagenetic processes, especially those related to fluid and gas circulation. Differences in methane seepage and hydrate occurrence could be due to spatial variations in methane fluid flow and pathways, leading to dynamic conditions at these sites with an impact on the sulfate reduction and anaerobic oxidation of methane rates. Authigenic magnetic mineralogy, mostly sensitive to biogeochemical processes at the sulfate–methane transition zone, would respond to fluid and gas flow variations, especially of methane.

1. Introduction

International Ocean Discovery Program (IODP) Expedition 385 took place in the Gulf of California, Mexico, to study Guaymas Basin tectonics and biosphere (**Teske et al.,** 2021a). Among the various scientific goals of this expedition, one primary objective was the study of subsurface microbial communities to assess carbon storage in high organic carbon–rich sediments and to understand conditions that limit life in hot and deep biosphere (Teske et al., 2018). Because iron Fe(III) is an essential element for microbial activity, documenting the magnetic mineral assemblages and investigating the distribution of the iron Fe(III)–bearing solid phases in the sediments will provide new insights into the Fe elemental cycle in Guaymas Basin.

In chemically reducing marine environments, such as in Guaymas Basin, detrital and authigenic iron (oxyhydr)oxides (e.g., magnetite [Fe_3O_4], hematite [Fe_2O_3], and goethite [α-FeOOH]) are used by microbes as electron acceptors to oxidize organic matter, releasing dissolved iron (Fe^{2+}) into pore water, which is called dissimilatory iron Fe(III) reduction (DIR) (e.g., Froelich et al., 1979; Lovley, 1991). During burial in sulfidic conditions, dissolved iron liberated by DIR and Fe(III)-bearing solid-phase (oxyhydr)oxides react with dissolved hydrogen sulfide (HS^-/H_2S) to form iron monosulfides (FeS), greigite (Fe_3S_4) and/or pyrite (FeS_2) (e.g., Jørgensen and Kasten, 2006; Jørgensen et al., 2019). Hydrogen sulfide is released during organoclastic sulfate reduction associated with organic matter decomposition (e.g., Berner, 1981; Jørgensen, 1982) and microbial anaerobic oxidation of methane (AOM) above and at the sulfate–methane transition zone (SMTZ) (e.g., Borowski et al., 1996; Knittel and Boetius, 2009; Treude et al., 2005). These biogeochemical processes strongly affect the iron-bearing magnetic minerals, which then affect the magnetic properties of sediments and sedimentary rocks (Roberts, 2015) and link the biogeochemical cycles of iron (Fe), sulfur (S), and carbon (C).

Iron Fe(III) reduction is an important mechanism for microbial respiration because microorganisms use Fe(III)-bearing minerals as electron acceptors during organic carbon degradation (e.g., Berner, 1981; Vargas et al., 1998). Köster et al. (2021) reported that in sediments of the Nankai Trough (Japan) high amounts of reducible Fe(III) can be preserved in phyllosilicates and can potentially serve as electron acceptors for microbial Fe reduction in the deep subseafloor sediments millions of years after deposition. Moreover, Kashefi and Lovely (2003) reported that Fe(III)-reducing microorganisms can grow under high-temperature and high-pressure conditions. These two studies show the potential for iron Fe(III) reduction to be an important reaction in settings with temperature close to the limit of life.

The study presented in this data report focuses on the characterization of Fe- and S-bearing mineral phases in biogenic sediments at two sites drilled near the Sonora margin, Sites U1549 and U1552 (Figure **F1**). Attenuated cold methane seepage conditions exist at Site U1549 in the central
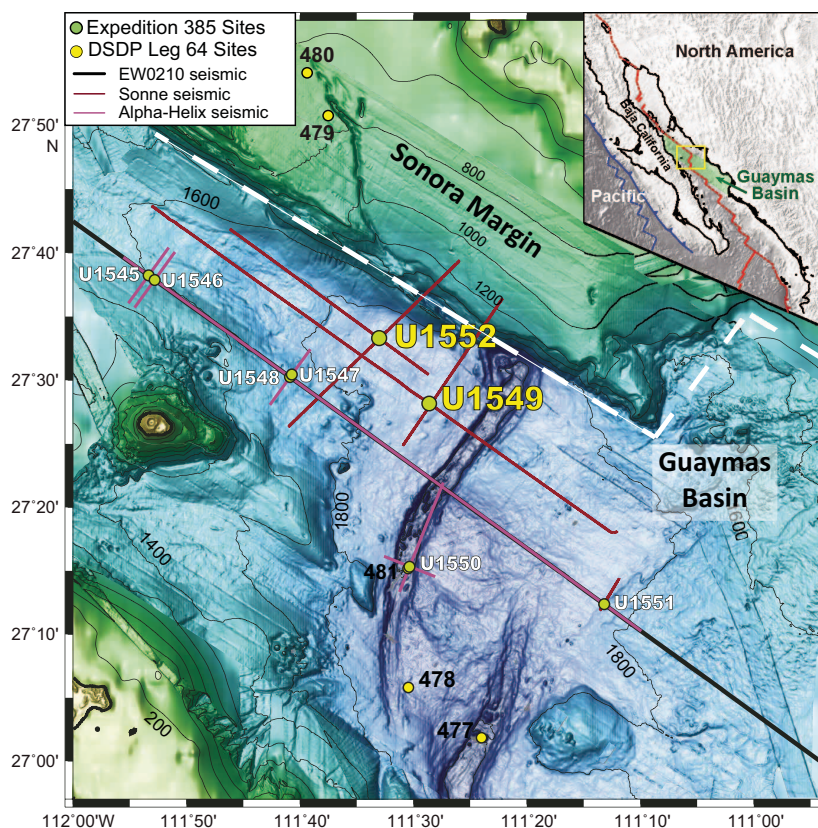

Figure F1. Location map of Expedition 385 sites in Guaymas Basin (modified from Teske et al., 2021a). DSDP = Deep Sea Drilling Project.

basin with methane appearance below 25 meters below seafloor (mbsf), and hydrate was found to be present from ~25 mbsf at Site U1552. These two sites, ~12 km apart, represent an opportunity to study the influence of gas hydrate occurrence on the magnetic mineralogy and different geothermal gradients in shallow young organic-rich sediments (<170 mbsf; <0.29 Ma; **Teske et al.**, 2021a). Rock magnetic measurements and Fe and S speciation were conducted to determine the iron- (carbonates and oxides) and sulfur- (sulfides and sulfates) bearing solid phases in associations with methane cold seepage and gas hydrates at these two sites.

2. Methods and materials

2.1. Methods

2.1.1. Rock magnetic analysis

All rock magnetic measurements were conducted at the Center for Advanced Marine Core Research, now the Marine Core Research Institute of Kochi University (Japan). Low-field, low-frequency (χ_{lf}) (0.465 kHz) measurements on oriented discrete samples were made with a MS2B Bartington Instruments magnetic susceptibility meter (field = 250 µT). The natural remanent magnetization (NRM) and an anhysteretic remanent magnetization (ARM) were measured with a 2G Enterprises 760R cryogenic magnetometer in a shielded paleomagnetic room. ARM was imparted in a direct current (DC) bias field of 50 µT in the presence of an 80 mT peak alternating field (AF). A saturation isothermal remanent magnetization (SIRM) was subsequently imparted to the samples along the +z direction at 1.2 T using a MMPM10 impulse magnetizer before being analyzed with a Natsuhara Giken spinner magnetometer. The samples were then remagnetized along the –z direction with a DC field of 0.3 T and were measured again to calculate the $S_{-0.3T}$ parameter ($S_{-0.3T} = [(-IRM_{-0.3T}/SIRM) + 1]/2$; Bloemendal et al., 1992), which indicates the relative proportion of high coercivity minerals in mixtures with soft ferrimagnetic minerals. Hysteresis loops with a maximum field of 1 T were measured on dry sediment powdered materials at room temperature with a Princeton Measurements Corporation vibrating sample magnetometer (VSM). The saturation magnetization (M_s), saturation remanent magnetization (M_r), and coercivity (B_c) were derived from the loops. Saturation was assumed above 70% of the maximum applied field, which might underestimate M_r/M_s (Roberts et al., 2018, and references therein). The coercivity of remanence (B_{cr}) was determined from backfield demagnetization curves of M_r. The parameter D_{JH} is derived from the hysteresis properties as the ratio of $D_{JH} = (M_r/M_s)/(B_{cr}/B_c)$ (Housen and Musgrave, 1996). First-order reversal curves (FORCs; Pike et al., 1999) were measured for 21 and 31 samples from Hole U1549B and Site U1552, respectively, selected at ~5–10 m stratigraphic intervals. A total of 91 FORCs per sample were measured with a 1 T saturating field (100 ms averaging time; 4 mT field increment). Regular FORC diagrams with evenly spaced field steps were processed using the FORCinel software (Harrison and Feinberg, 2008), with a constant smoothing factor (SF).

Low-temperature magnetic measurements (300–10 K) were made with a Quantum Design Magnetic Properties Measurement System (MPMS) for 10 and 11 selected samples from Holes U1549B and U1552C, respectively. The samples each have ~100–120 mg mass and were dried, ground lightly to a fine powder, and sealed in a gelatin capsule before being measured. A room-temperature SIRM (RT-SIRM) was acquired at 2.5 T. A 300–10–300 K cooling-warming cycle of the RT-SIRM was then carried out in zero magnetic field (<20 µT) trapped within the MPMS. A low-temperature SIRM (LT-SIRM) was imparted at 10 K at 2.5 T, and samples were then warmed to room temperature in zero magnetic field and measured (termed "zero-field-cooled" [ZFC]). Samples were subsequently cooled to 10 K in a 2.5 T magnetic field and the LT-SIRM was analyzed while warming to 300 K (termed "field-cooled" [FC]). Thermomagnetic experiments in vacuum were made on 16 and 14 selected specimens from Holes U1549B and U1552C, respectively, with a Natsuhara Giken NMB-89 magnetic balance from room temperature to 700°C (at a heating rate of 10°C/min in a 0.3 T field).

2.1.2. Iron and sulfur speciation

The different mineral phases containing iron were extracted from dry and ground sediments by a 3-step sequential extraction derived from a 7-step extraction method described by Poulton and Canfield (2005) and Gott (2016). The first step aimed to extract iron associated with carbonate phases (Fe_{ac}) including siderite [$FeCO_3$] and ankerite/ferrodolomite [$Ca(Fe,Ca,Mg,Mn)(CO_3)_2$]. This extraction was performed using a 1 M sodium acetate solution buffered with acetic acid to pH 4.5 added to a known mass of dry sediment (ratio solution/sediment of 50) and agitated for 24 h at room temperature. The second step extracted iron in association with crystalline oxides (Fe_{dith}) such as goethite (α-FeOOH) and hematite (α-Fe_2O_3). This extraction was performed using a 50 g/L sodium dithionite solution buffered with 0.35 M acetic acid and 0.2 M sodium citrate to pH 4.8 added to the remaining sediment and agitated 2 h at room temperature. The third and last step extracted iron in magnetite (Fe_{ox}) and was performed using a 0.2 M ammonium oxalate, 0.17 M oxalic acid solution buffered with ammonium hydroxide to pH 3.2 added to the remaining sediment and agitated 6 h at room temperature. Between each step, the tubes were centrifuged at 3000 rpm for 15 min and the decantation extract was filtered and transferred into another tube. This 3-step extraction produced samples from three different matrixes. The samples are diluted 10, 10, and 2 times, respectively, before being analyzed by inductively coupled plasma–atomic emission spectrometry (ICP-AES) to measure iron concentrations in each of these matrixes. Yet, these dilutions are not sufficient to avoid a matrix effect because of the large amount of salts contained in these solutions. Standards were then prepared for each matrix in the same conditions as the samples using SCP Science PlasmaCAL P and Mn and VWR Chemicals Al and Fe 1000 ppm stock solutions. Analyses were performed using an ICP-AES spectrometer (Horiba Jobin Yvon Ultima 2) at the Pôle Spectrométrie Océan in Brest, France (PSO), and final concentrations in the sediments were calculated from these results, the mass of sediment weighted corrected for salt content, the volume of extractant used, and the dilution factors. The repeatability of this method was demonstrated by the analysis of an environmental certified sediment: Canadian Reference Material MESS-4 (Willie et al., 2014), with an error of less than 7% overall.

Solid-phase sulfide extractions were carried out on ~0.5 g of dry and ground sediment in glass flasks under a nitrogen atmosphere. All solutions used for extractions and added in the flasks were first flushed with nitrogen for 30 min. An aliquot of 10 mL of ethanol was added to the flasks to humidify the samples and purged again for 10 min to flush the oxygen from the system. Acid volatile sulfides (AVS), mainly sulfides contained in FeS, were extracted using 6 M HCl for 1 h (Gott, 2016), and the H_2S produced by the extraction was trapped as an Ag_2S precipitate in a test tube filled with about 12 mL of $AgNO_3$ 3% and NH_4OH 10% solution to prevent the formation of AgCl (Carmody et al., 1998). Once the AVS was extracted, the $AgNO_3$ trap was replaced by a new one. Chromium reducible sulfur (CRS), mainly sulfur contained in pyrite, was extracted in the same flasks after the addition of 20 mL of 1 M $CrCl_2$ and 10 mL of 12 M HCl (Canfield et al., 1986; Gott, 2016). The mixture was then boiled and allowed to react for 2 h, with the vapor phase cooled down by a constant tap water circulation. To quantify the concentration of AVS and CRS, the Ag_2S precipitates were filtered, rinsed with water and acetone, and dried in an oven at 60°C for 30 min before being weighed in a weighing paper. The fraction of Fe associated with pyrite (Fe_{PY}) was calculated using a molar ratio of 1 mol of Fe for 2 mol of S (FeS_2). To control the accuracy of this method, the marine shale sample WHIT with a CRS value of 2.262 ± 0.100% (Alcott et al., 2020) was used as a standard. For a total of two runs, the WHIT CRS value found was 2.258 ± 0.009%. Based on six replicates, the repeatability of the method was around 1.0%. The degree of pyritization (DOP) was calculated from the percentages obtained from the different extractions (Brocławik et al., 2020) as

$$DOP = Fe_{PY}/Fe_{HR},$$

where Fe_{HR} is the highly reactive fraction of iron (Raiswell and Canfield, 2012) defined as

$$Fe_{HR} = Fe_{PY} + Fe_{ac} + Fe_{dith} + Fe_{ox}.$$

2.2. Materials

2.2.1. Site U1549

Site U1549 is located ~9.5 km northwest of the northern axial graben of Guaymas Basin (Figure **F1**) and ~780 m northwest of Octopus Mound, a mound-shaped seafloor feature where active cold-seep communities were documented by preexpedition site surveys (Teske et al., 2021d). An underlying sill at ~450 mbsf is thought to be present and indicates gas movement along and around a pipe structure.

Sediments recovered are late to middle Pleistocene and are mostly biogenic (mainly diatom ooze) with a significant (~10%) proportion of sand- to silt-sized siliciclastic components (**Teske et al.,** 2021b). Three ~5 m thick and one ~1.5 m thick gravity-flow deposits were identified. Based on shipboard paleomagnetic results, Hole U1549A cores were assigned to the normal Brunhes Chron C1n (younger than 0.78 Ma). Pore water analysis indicates the SMTZ is at 30 mbsf in Hole U1549A and 25 mbsf in Hole U1549B (**Teske et al.,** 2021b).

For this study, 41 oriented discrete samples (7 cm^3 top-oriented plastic cubes) were collected from Hole U1549A sediment cores from ~1 to 159.4 mbsf (Cores 1H–18H) and 67 discrete samples (nonoriented material) were collected from Hole U1549B from 1.4 to 164.8 mbsf (Cores 1H–18H).

2.2.2. Site U1552

Site U1552 is located ~20 km northwest of the northern axial graben in Guaymas Basin, proximal to the Sonora margin (Figure **F1**). The site is adjacent to a mostly buried mound that presents a structure similar to the surficial mound near Site U1549 and where gas hydrate is present on the seafloor. The age and lithologies identified at Site U1552 are similar to Site U1549 with mainly diatom clay and alternating silty clay and sandy silt.

Site U1552 differs from Site U1549 by the presence of gas hydrates identified between 25 and 45 mbsf (**Teske et al.,** 2021a). Gas hydrates found at Site U1552 are more likely disseminated low-concentration hydrate (Type I) or most likely concentrated hydrates in sand-rich intervals (Type V) (**Teske et al.,** 2021c).

Sulfate (SO_4^{2-}) concentration decreases in the uppermost 10 m and remains low, below 0.5 mM below this depth in all holes. In Holes U1552A and U1552B, erratically high methane concentrations could be related to the presence of gas hydrates. Based on the sulfate profile and an increase in methane, the SMTZ is estimated to be around 10 mbsf (**Teske et al.,** 2021c). The downhole variations of selected elements and methane are presented in Figures **F9** and **F10** for Holes U1552A and U1552C, respectively.

For this study, 20 oriented discrete samples (7 cm^3 top-oriented plastic cubes) were collected from ~2.3 to ~102.7 mbsf (Cores 385-U1552A-1H through 12H) and 38 discrete samples (nonoriented material) were collected from 0.7 to 104.3 mbsf (Cores 1H–12H) in Hole U1552A sediment cores. A total of 10 oriented discrete samples (7 cm^3 top-oriented plastic cubes) were collected from 8.1 to 95.0 mbsf (Cores 385-U1552C-2H through 11H) and 41 discrete samples (nonoriented material) were collected from 0.8 to 97.8 mbsf (Cores 1H–11H) were collected in Hole U1552C sediment cores.

3. Results

3.1. Downhole magnetic properties

3.1.1. Site U1549

Concentration-dependent parameters, NRM, magnetic susceptibility χ_{lf}, ARM, and SIRM, do not show significant downhole variations, except in siliciclastic-dominated depositional units where parameter values are more than one order of magnitude higher than the average background values of the clay-rich diatom ooze and diatom clay (Figure **F2A–F2D**; Table **T1**). The magnetic properties trend likely reflects higher terrigenous inputs in coarser lithologies (**Persad and Marsaglia**, 2023).

Magnetic grain size proxies, ARM/χ_{lf} and ARM/SIRM, support these results and have lower values in the siliciclastic deposition units (Figure **F2E, F2F**; Table **T1**). In clay-rich diatom ooze and diatom clay, these two proxies show higher values indicating finer magnetic grains (Lu and Banerjee, 1994), except for ARM/χ_{lf} below 100 mbsf, which has values similar to the siliciclastic deposition units.

$S_{-0.3T}$, a proxy for the relative abundance of high-coercivity minerals in a mixture with low-coercivity minerals, is quasiconstant downhole with values around 0.92, except above 20 mbsf and in some isolated intervals (Figure **F2G**; Table **T1**). The high value of $S_{-0.3T}$ suggests that the magnetic mineralogy of the studied sediments is dominated by low-coercivity minerals, such as magnetite. $S_{-0.3T}$ decreases very rapidly from 0.91 to 0.84 in the first 6 m below the surface, indicating that the low-coercivity fine-grained magnetic fraction (e.g., magnetite) is preferentially dissolved in this interval (e.g., Karlin, 1990; Leslie et al., 1990). The higher coercivity fraction (e.g., hematite) is better preserved, as suggested by lower $S_{-0.3T}$ values.

SIRM/χ_{lf} is sometimes used as a proxy of single-domain (SD) greigite particles (e.g., Roberts et al., 2011; Larrasoaña et al., 2007) with increased values indicating the presence of iron sulfides. SIRM/χ_{lf} values are scattered from the surface to ~40 mbsf and never exceed 30 kA/m (Figure **F2H**; Table **T1**). This indicates a complex magnetic mineral assemblage with different mineralogy coercivity (e.g., magnetite versus greigite) and magnetic grain size (fine versus coarser particles) in
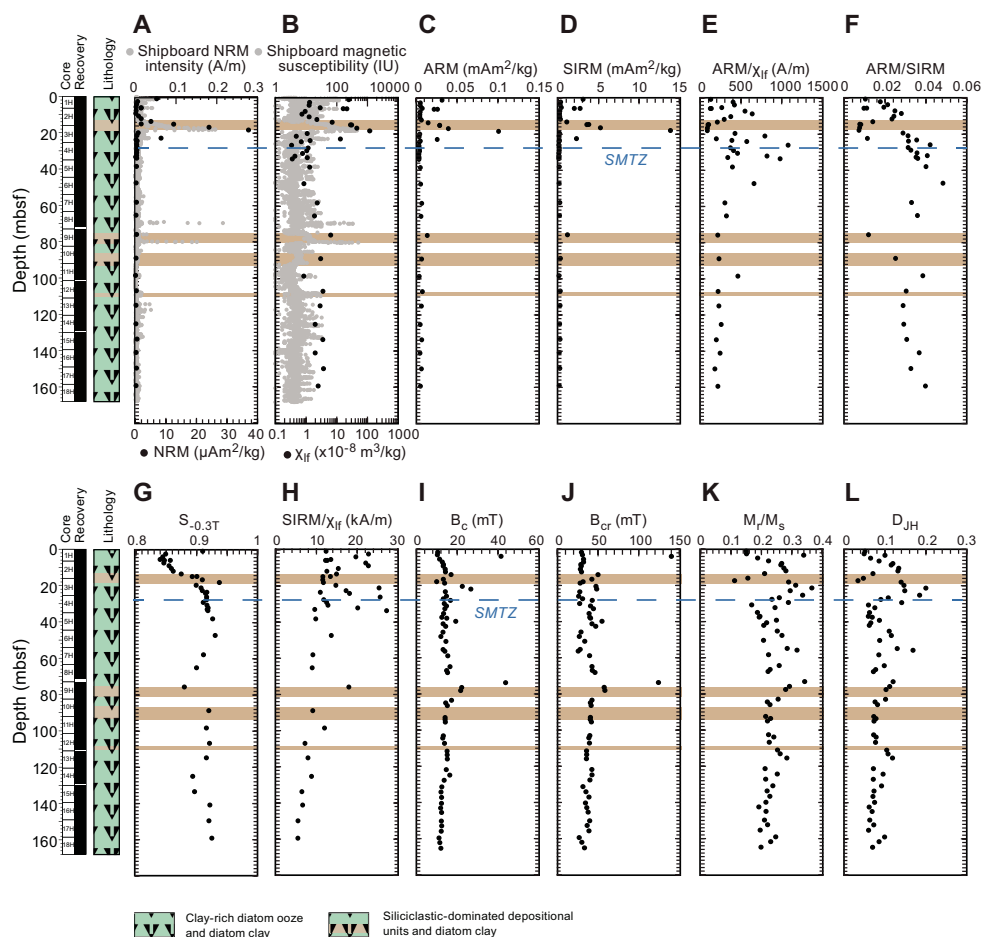

Figure F2. Downhole rock magnetic properties of sediment samples, Site U1549. Shipboard data are from Hole U1549A archive section half measurements. A–H. Hole U1549A oriented samples. I–L. Hole U1549B nonoriented material. SMTZ at ~28 mbsf.

Table T1. Rock magnetic properties measured on oriented cube samples, Site U1549. **Download table in CSV format.**

shallower sediments above the SMTZ. Overall, SIRM/χ_{lf} decreases progressively downhole, which suggests a progressive reduction of SD minerals with depth. This trend may reflect a progressive pyritization of greigite with depth, as well as a shift toward lower coercivity minerals such as multidomain (MD) grains because finer grains are preferentially dissolved/reduced in sediments (e.g., Musgrave et al., 2019).

The coercivity (B_c) and remanent coercivity (B_{cr}) of discrete samples do not vary significantly with depth with an average of 14.8 ± 5.6 mT and 40.5 ± 17.8 mT, respectively (Figure **F2I, F2J**; Table **T2**). These values are typical of low-coercivity SD particles, such as magnetite. Two samples have higher B_c and B_{cr} values, similar to what is found for high-coercivity iron sulfides (greigite and pyrrhotite) and iron oxides (e.g., hematite). Hysteresis parameters ratios, M_r/M_s and D_{JH}, mimic each other downhole with an alternation of higher and lower values (Figure **F2K, F2L**; Table **T2**). Higher values of these ratios may reflect a better preservation of SD magnetic particles in these intervals or formation of a new magnetic phase due to localized fluid circulation (Musgrave et al., 2019).

3.1.2. Site U1552

Downhole magnetic properties of Holes U1552A and U1552C are shown in Figures **F3** and **F4**, respectively. Nonrecovery is due to the presence of gas hydrates at this site (**Teske et al.**, 2021a).

As at Site U1549, NRM and magnetic susceptibility decrease drastically in shallower sediments and remain at low values to the bottom of Holes U1552A and U1552C (Figures **F3A, F3B, F4A,**

Table T2. Hysteresis properties measured on nonoriented material, Site U1549. **Download table in CSV format.**
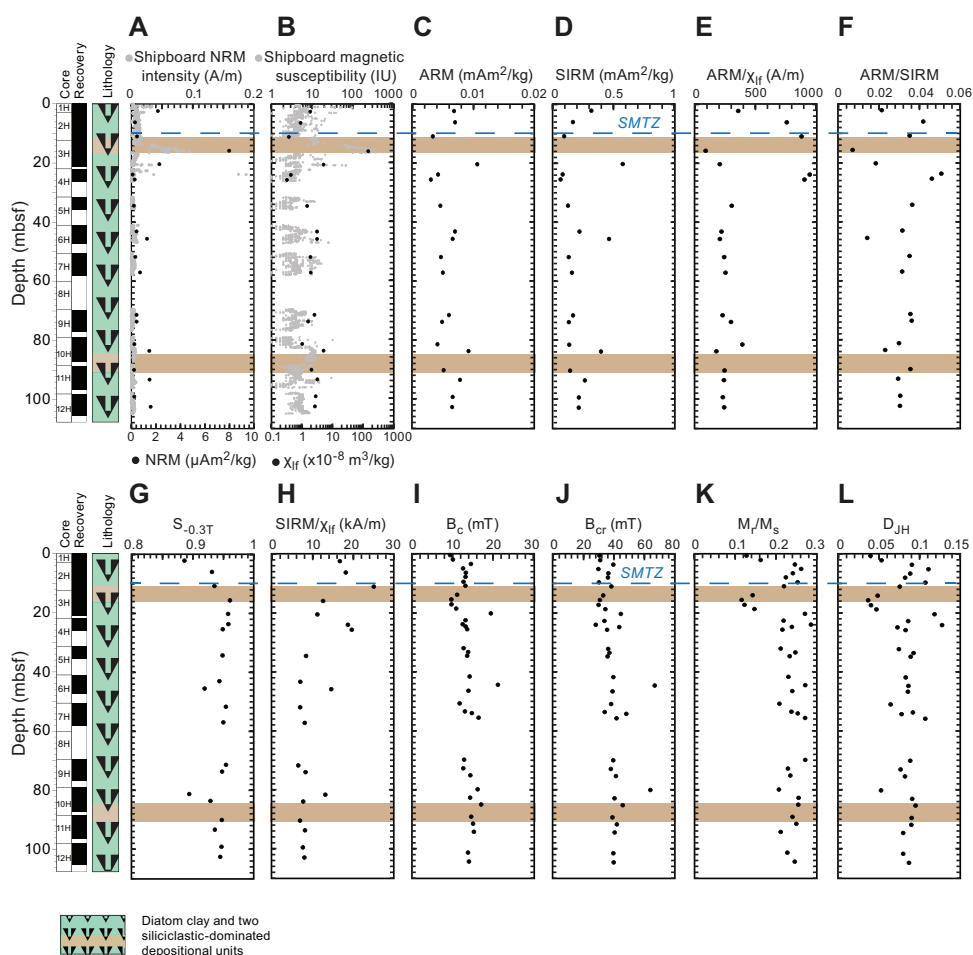

Figure F3. A–L. Downhole rock magnetic properties of sediment samples, Hole U1552A. Shipboard data are from archive section half measurements. SMTZ at ~10 mbsf.

F4B; Table **T3**). Exceptions with higher values are for the siliciclastic deposition units. The two other proxies for magnetic mineral concentration, ARM and SIRM, mimic each other and support a lower magnetic mineral concentration below ~5 mbsf in diatom clay sediments (Figures **F3C, F3D, F4C, F4D**; Table **T3**).

Grain size proxies, ARM/χ_{lf} and ARM/SIRM, for Hole U1552A have scattered values above ~30 mbsf and do not vary significantly below this depth (Figure **F3E, F3F**; Table **T3**). Below ~30 mbsf, these two ratios stay nearly constant with values similar to those measured at Site U1549. The sampling resolution for Hole U1552C is lower than the resolution for Hole U1552A; therefore, the downhole variations of ARM/χ_{lf} and ARM/SIRM are less marked (Figure **F4E, F4F**; Table **T3**). Nevertheless, one can assume the same trend with scattered values above ~30 mbsf and nearly constant values below.

$S_{-0.3T}$ has high values, averaging 0.94 ± 0.02 and 0.95 ± 0.01 for Holes U1552A and U1552C, respectively (Figures **F3G, F4G**; Table **T3**). As at Site U1549, these high values indicate a magnetic mineral assemblage dominated by low-coercivity minerals. Lower values would indicate a relatively more important abundance of higher coercivity magnetic minerals in the magnetic assemblage.

SIRM/χ_{lf} at Site U1552 shows a trend comparable to that at Site U1549 with scattered values above ~25–30 mbsf. The ratio then progressively decreases downhole with bottom values below 10 kA/m (Figures **F3H, F4H**; Table **T3**). This would suggest a progressive downhole pyritization with the dissolution/reduction of iron oxides to form pyrite.
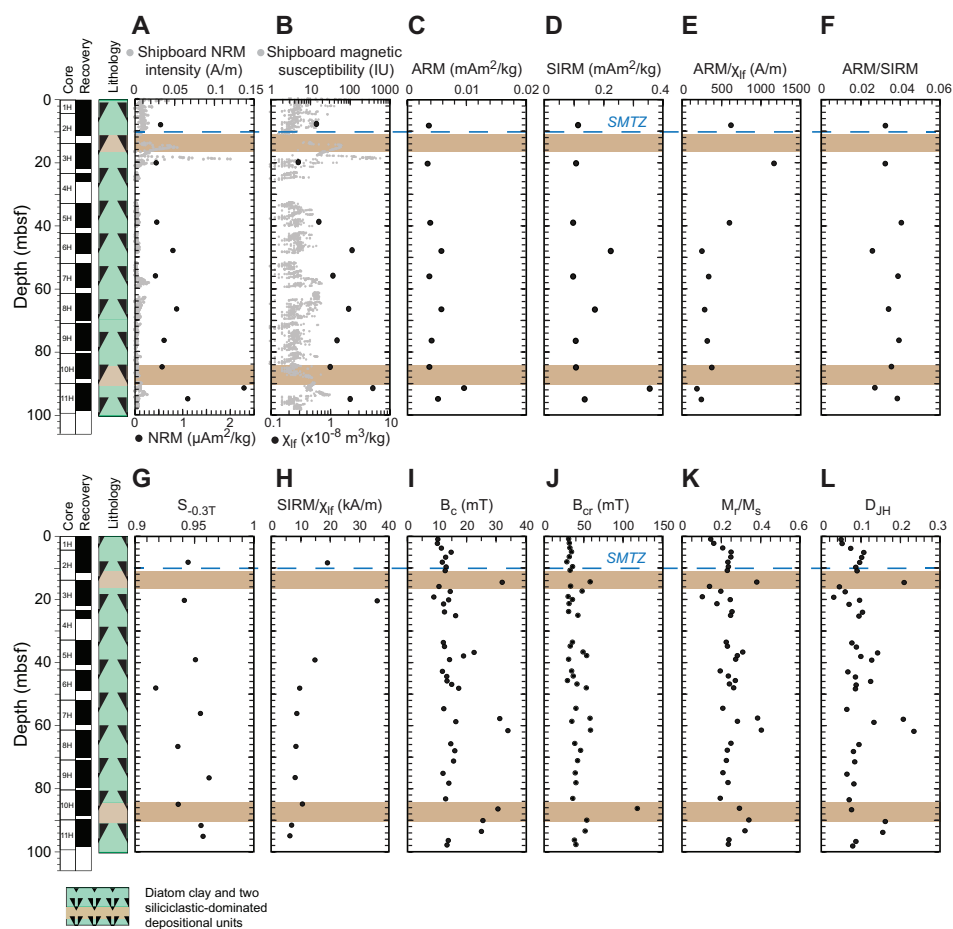

Figure F4. A–L. Downhole rock magnetic properties of sediment samples, Hole U1552C. Shipboard data are from archive section half measurements. SMTZ at ~10 mbsf.

Table T3. Rock magnetic properties measured on oriented cube samples, Site U1552. **Download table in CSV format.**

As at Site U1549, hysteresis properties of samples from Site U1552 mimic each other. B_c and B_{cr} have similar downhole variations with average values of 13.7 ± 2.4 and 38.7 ± 7.9 mT for Hole U1552A and 16.1 ± 6.3 and 41.5 ± 14.9 mT for Hole U1552C (Figures **F3I, F3J**, **F4I, F4J**; Table **T4**). These values are in the same range as those Site U1549, supporting low-coercivity minerals such as magnetite as the dominant magnetic phase in the samples. Higher values would reflect the presence of other magnetic phase(s). M_r/M_s and D_{JH}, as at Site U1549, mimic each other downhole with lows and highs possibly reflecting changes in the magnetic mineral assemblage because of fluid circulation and gas migration within the sediment (Figures **F3K, F3L**, **F4K, F4L**; Table **T4**).

3.2. Magnetic mineralogy analysis

3.2.1. Site U1549

A series of rock magnetic analyses were performed to characterize the magnetic mineral assemblage of the samples.

Low-temperature magnetic measurements showed overall similar downhole patterns. LT-SIRM for both ZFC and FC curves decreased drastically by more than 50% below 30 K, suggesting the presence of superparamagnetic grains (Passier and Dekkers, 2002), and progressively continued to decrease to 300 K (Figure **F5A, F5F, F5K, F5P**). The ZFC and FC curves are quasisuperimposed, suggesting that very small, superparamagnetic particles do not dominate the FC LT-SIRM. A decrease in magnetization on both ZFC and FC curves is observed at around 110–120 K, corre-

Table T4. Hysteresis properties measured on nonoriented material, Site U1552. **Download table in CSV format.**
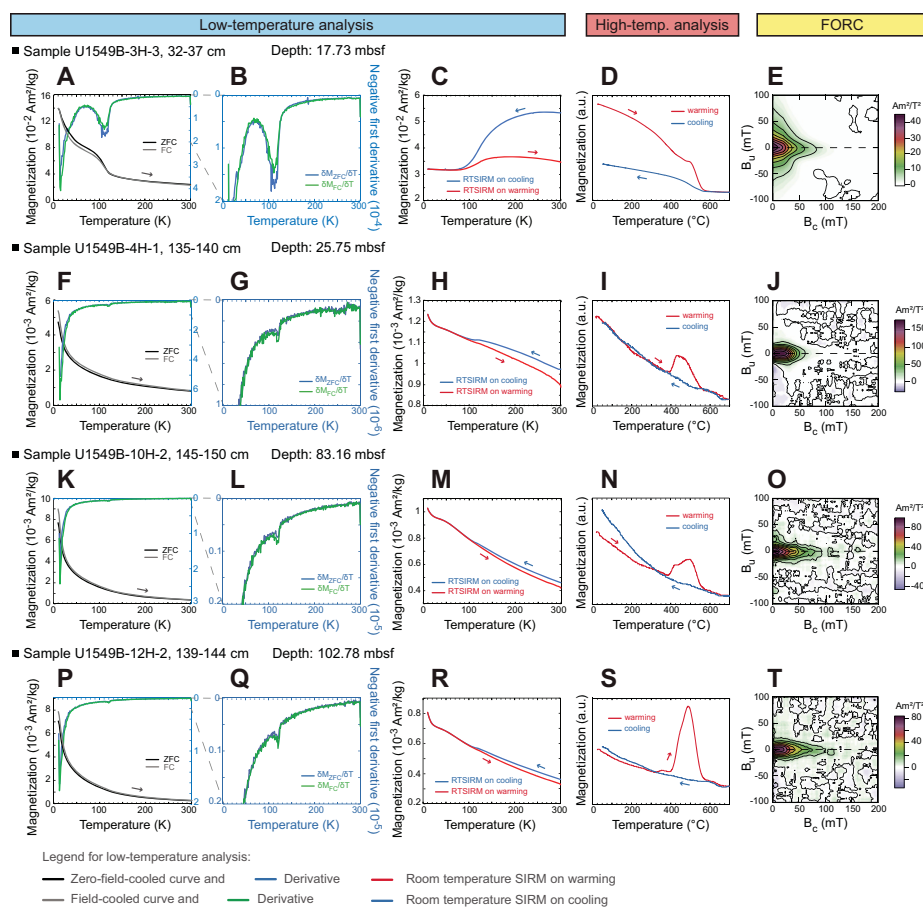

Figure F5. Rock magnetic measurements on selected samples, Hole U1549B. A, F, K, P. ZFC and FC curves. B, G, L, Q. First derivatives. C, H, M, R. RT-SIRM during cooling and warming. D, I, N, S. Thermomagnetic curves during in-field warming and cooling cycle. E, J, O, T. FORC diagrams.

sponding to the temperature of the Verwey transition of magnetite, which changes its symmetry from cubic to monoclinic (e.g., Muxworthy and McClelland, 2000; Özdemir et al., 2002). This is better seen on shallower samples (e.g., Figure **F5A**) and by calculating the first derivative of ZFC and FC LT-SIRM (Figure **F5B, F5G, F5L, F5Q**). The same observation can be obtained from the RT-SIRM demagnetization with the Verwey transition identified in all analyzed samples (Figure **F5C, F5H, F5M, F5R**). The Verwey transition is less marked for deeper samples. RT-SIRM on warming is not superimposed with the RT-SIRM on cooling, indicating that part of the magnetization was lost through the Verwey transition, likely due to single-vortex (SV) or MD magnetite grains (e.g., Özdemir et al., 2002).

The thermomagnetic curves acquired at high temperature supports the presence of magnetite in all analyzed samples with an important decrease in magnetization at 570°–580°C (Figure **F5D, F5I, F5N, F5S**) (Dunlop and Özdemir, 1997). During warming, most samples show an increase in magnetization between 350° and 400°C (e.g., Figure **F5I, F5N, F5S**), which may suggest that a mineral phase existing in the samples had been altered to form another phase carrying magnetization. This may be related to the destabilization of paramagnetic iron sulfides present in the samples (e.g., pyrite), which transform into ferrimagnetic magnetite while heating (e.g., Passier et al., 2001; van Baak et al., 2016). Hematite, characterized by a decrease in magnetization at 670°C (Dunlop and Özdemir, 1997), is also identified in the samples (e.g., Figure **F5I, F5S**). Hematite might be either originally present in the samples or formed during the experiment from the alteration of magnetite (van Velzen and Zijderveld, 1992).

The FORC diagrams indicate that a low-coercivity, mostly interacting phase with a B_c peak at around 10 mT dominates the FORC signature (Figure **F5J, F5O, F5T**). This is likely small SD grains of magnetite, possibly combined with MD grains (e.g., Muxworthy and Dunlop, 2002; Roberts et al., 2000). The FORC diagram of the sample in Figure **F5E**, however, has triangular contours, suggesting the presence of noninteracting coarser grains, possibly SV iron oxides (e.g., Lascu et al., 2018; Roberts et al., 2017), in addition to finer SD grains.

3.2.2. Site U1552

Generally, the magnetic mineral assemblage characterized in Site U1552 samples is similar to the assemblage characterized at Site U1549, with one significant difference discussed below.

The low-temperature magnetic measurements, ZFC, FC, and RT-SIRM curves, all indicate the presence of magnetite with a Verwey transition at 110–120 K (Figure **F6A–F6C, F6F–F6H, F6K–F6M, F6P–F6R**) (e.g., Muxworthy and McClelland, 2000; Özdemir et al., 2002). No other magnetic phase can be identified from the low-temperature measurements.

The thermomagnetic curves of the samples from Site U1552, as at Site U1549, indicate a complex magnetic mineral assemblage with different magnetic phases. Overall while heating, the magnetization decreases but increases more or less importantly at about 400°C before decreasing to ~570°–580°C and then ~650°C (Figure **F6D, F6I, F6N, F6S**). These results support an assemblage that consists of a magnetic phase forming while heating (likely iron sulfides to magnetite) magnetite and hematite (Dunlop and Özdemir, 1997). By contrast to Site U1549, a few samples exhibit an additional feature with a change-in-slope in the warming curve at around 250°C. This is the case with the sample in Figure **F6I**.

The FORC diagram associated with this sample (Figure **F6J**) is different from the other diagrams (Figure **F6E, F6O, F6T**) because it has a higher peak coercivity (B_c) at around 50–60 mT and well-defined concentric contours with a negative region in the lower left corner of the diagram indicating SD high-coercivity grains. This type of FORC diagram is typical of interacting SD greigite (e.g., Roberts et al., 2006, 2011). The FORC diagram in Figure **F6J** is very similar to what was previously reported in greigite-bearing sediments (e.g., Kars and Kodama, 2015a, 2015b; Kars et al., 2021a, 2021b). This observation combined with the decrease in magnetization at ~250°C (Figure **F6I**) suggests that greigite, too, is a magnetic mineral present in samples from Site U1552. The high-coercivity ferrimagnetic iron sulfide was also identified in other analyzed Site U1552 samples. However, it has not been identified in the rock magnetic data set from Site U1549, although the

decrease in magnetization around 200°C for the sample shown in Figure **F5I** may indicate the presence of greigite.

3.3. Iron and sulfur speciation

3.3.1. Site U1549

Before presenting the iron and sulfur speciation data, a reminder about a few shipboard results for sulfate, sulfide, and iron from the interstitial water analysis, together with methane concentrations, is necessary. Sulfate concentration decreases from 28 to 5 mM in the uppermost 30 m at Site U1549 and remains below 0.5 mM below this depth (Figure **F7A**) (**Teske et al.**, 2021b). Headspace methane concentrations sharply increase just below 25 mbsf to reach a maximum value of 8.82 mM at ~35 mbsf (Figure **F7A**). Methane levels then decrease downhole to a minimum of ~1.5 mM to the deepest sample at 159.1 mbsf in Hole U1549B. Therefore, the SMTZ is estimated to be at around 25–30 mbsf (**Teske et al.**, 2021b). Sulfide ($\Sigma H_2S = S_2 + HS^- + H_2S$) concentration presents a maximum of 5.8 mM at 28 mbsf that corresponds to the SMTZ (Figure **F7A**) (**Teske et al.**, 2021b).

Iron ($Fe = Fe^{2+} + Fe^{3+}$) concentration in pore water remains <7 µM to 55 mbsf, reaches a maximum value of 53 µM in Hole U1549B, and decreases to <15 µM farther downhole (Figure **F7B**; Table **T5**) (**Teske et al.**, 2021b). Results of iron speciation on the solid phase show similar downhole variations with values between 1.5 and 50.9 µmol/g for Fe_{ac}, 6.4 and 40.8 µmol/g for Fe_{dith}, and 7.9 and 39.1 µmol/g for Fe_{ox} in Hole U1549B (Figure **F7B**, **F7C**; Table **T5**). Maximum Fe_{ac}, Fe_{dith}, and Fe_{ox} values are found at 75.4 mbsf. Peaks of Fe_{ac}, Fe_{dith}, and Fe_{ox} correspond to peaks in total iron Fe_T (**Pastor et al.**, 2023) but still represent a minor fraction, around 10% (Figure **F7C**). Fe_T peaks
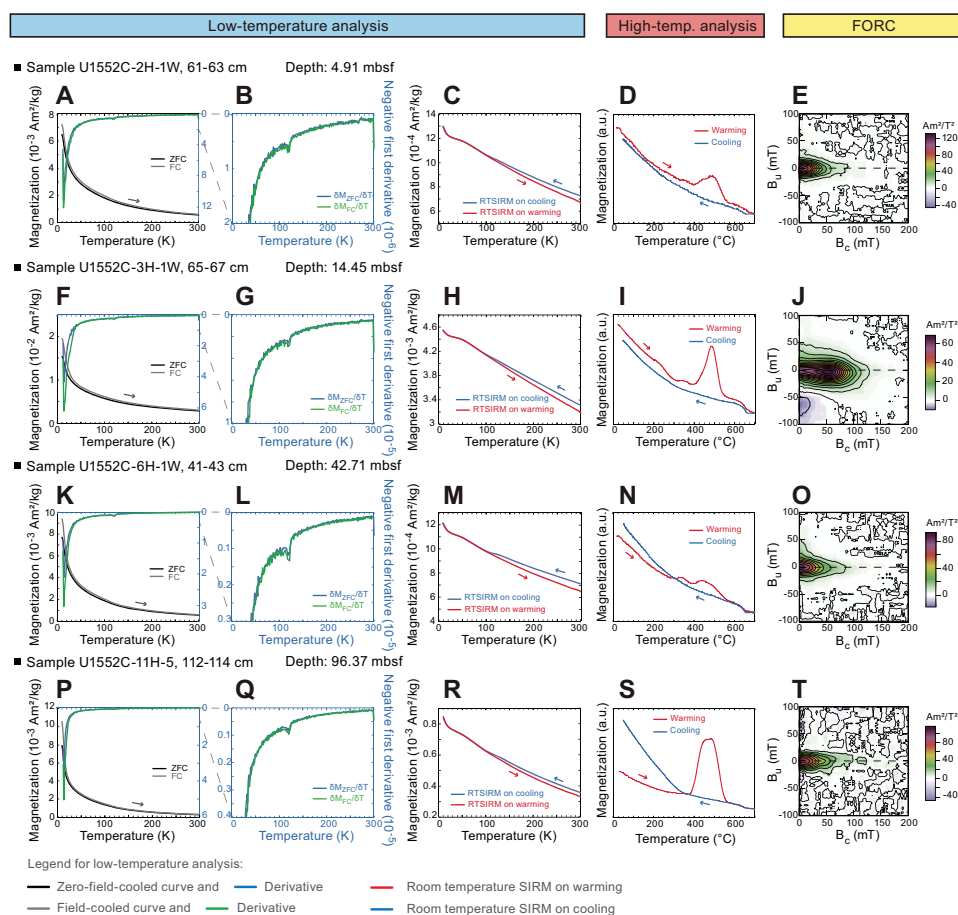

Figure F6. Rock magnetic measurements on selected samples, Hole U1552C. A, F, K, P. ZFC and FC curves. B, G, L, Q. First derivatives. C, H, M, R. RT-SIRM during cooling and warming. D, I, N, S. Thermomagnetic curves during in-field warming and cooling cycle. E, J, O, T. FORC diagrams.

are generally associated with peaks of iron in the form of pyrite (Fe_{PY}), with F_{PY} between 0.63% and 1.87% (Figure **F7C, F7D**; Table **T5**). The total amount of highly reactive iron (Fe_{HR}) represents less than half of the total iron present in the analyzed samples (Figure **F8A**). The Fe_{HR}/Fe_T value is generally above 0.38 (Figure **F8B**), which indicates an enrichment in reactive iron in the analyzed samples (Poulton and Raiswell, 2002).
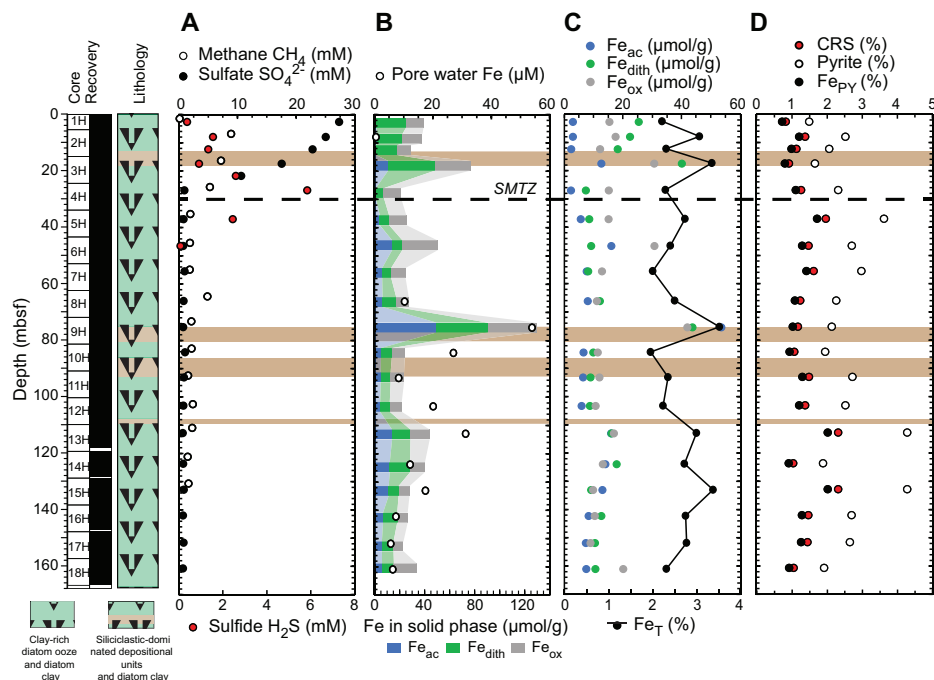

Figure F7. Downhole selected pore water properties and iron and sulfur speciation results, Hole U1549B. A. Pore water sulfate, dissolved sulfide, and methane concentrations. B. Dissolved iron (Fe^{2+}) in pore water and cumulative iron concentrations in solid phases extracted with acetate (Fe_{ac}), dithionite (Fe_{dith}), and oxalate (Fe_{ox}). C. Iron concentrations in solid phases extracted with acetate, dithionite, and oxalate, with total iron (Fe_T). D. Percentage concentrations of CRS, pyrite, and iron in form of pyrite. SMTZ at ~28 mbsf.

Table T5. Iron and sulfur speciation results, Site U1549. **Download table in CSV format.**
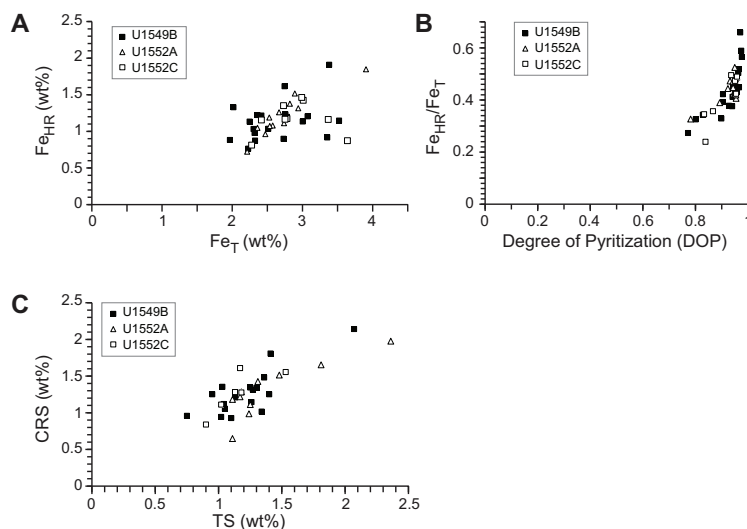

Figure F8. A–C. Selected cross-plots from iron and sulfur speciation results, Holes U1549B, U1552A, and U1552C. Data in A are from Pastor et al. (2023).

AVS (e.g., greigite) were detected but were not quantifiable. CRS values range 0.59%–2.14% with minima recorded at 17.4, 84.3, and 123.9 mbsf and the peak value at 133 mbsf (Figure **F7D**; Table **T5**). Generally, CRS values are similar to the total sulfur (TS) contents measured in the samples (**Teske et al.**, 2021b), with a CRS/TS value around 1, suggesting that most of the mineral sulfur fraction is in the pyrite form (Figure **F8C**). DOP varies between 0.77 and 0.98 (Figure **F8B**), with minima found where Fe_{ac}, Fe_{dith}, and Fe_{ox} are higher. DOP is a proxy that is used to estimate the proportion of Fe_{HR} initially present in the sediments that react to form pyrite. At Site U1549, DOP is very high, indicating an efficient pyritization process with potential limitation by iron oxides.

3.3.2. Site U1552

There is no significant difference in interstitial water analysis between Sites U1549 and U1552. Sulfate concentration decreases from 28 to <0.5 mM in the uppermost 10 m and remains <0.5 mM in all Site U1552 holes below this depth (Figures **F9A**, **F10A**) (**Teske et al.**, 2021c). Headspace methane concentrations increase markedly with values above 8 mM around 9 mbsf (Figures **F9A**, **F10A**). Erratically high methane concentrations were observed between 6 and 26 mbsf, and a maximum value of 93.1 mM was measured at 26 mbsf in Hole U1552A, where gas hydrates were recovered (Figure **F9A**) (**Teske et al.**, 2021c). In Hole U1552C, methane concentration reaches a maximum value of 7 mM at 16.7 mbsf before decreasing downhole to 0.7 mM (Figure **F9A**) (**Teske et al.**, 2021c). The SMTZ is estimated to be at around 10 mbsf at Site U1552. The sulfide (ΣH_2S) concentration maximum of 6.8 mM is at 6 mbsf, and concentrations are <10 µM below 16 mbsf (Figure **F9A**) (**Teske et al.**, 2021c). The interval exhibiting the maximum sulfide concentration is consistent with the SMTZ.

The concentration of pore water iron reaches maximum values of 76 µM at 17 mbsf, with a second peak at 53 mbsf in Hole U1552A (Figure **F9B**; Table **T6**), and 35 µM at 36 mbsf in Hole U1552C (Figure **F10B**; Table **T6**) (**Teske et al.**, 2021c). Below these depths, iron concentration steadily decreases downhole. At Site U1552, solid-phase iron components Fe_{ac}, Fe_{dith}, and Fe_{ox}, with both Holes U1552A and U1552C considered, present comparable downhole variations with values ranging 1.6–66.1, 7.8–41.2, and 10.0–142.7 µmol/g, respectively (Figures **F9B, F9C, F10B, F10C**;
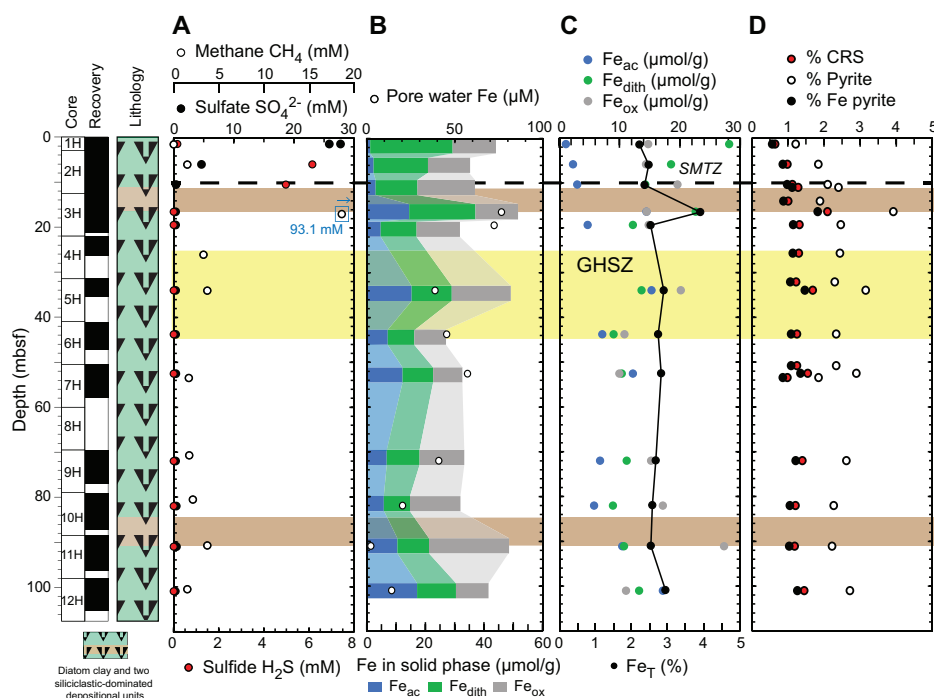

Figure F9. Downhole selected pore water properties and iron and sulfur speciation results, Hole U1552A. A. Pore water sulfate, dissolved sulfide, and methane concentrations. B. Dissolved iron (Fe^{2+}) in pore water and cumulative iron concentrations in solid phases extracted with acetate (Fe_{ac}), dithionite (Fe_{dith}), and oxalate (Fe_{ox}). C. Iron concentrations in solid phases extracted with acetate, dithionite, and oxalate, with total iron (Fe_T). D. Percentage concentrations of CRS, pyrite, and iron in form of pyrite. SMTZ at ~10 mbsf. Yellow = gas hydrate stability zone (GHSZ) between (25–45 mbsf).

Table **T6**). Fe$_{ac}$, Fe$_{dith}$, and Fe$_{ox}$ are generally lower in Hole U1552A compared to Hole U1552C (Figures **F9B, F10B**). Peaks of Fe$_{ac}$, Fe$_{dith}$, and Fe$_{ox}$ are found at 16.7, 64.2, and 92.6 mbsf in Hole U1552C (Figure **F10B, F10C**), respectively. It is overall less variable in Hole U1552A, with slightly higher contents found in shallower samples and in the gas hydrate zone (Figure **F9B, F9C**). As at Site U1549, peaks of Fe$_{ac}$, Fe$_{dith}$, and Fe$_{ox}$ correspond to peaks in Fe$_T$ (**Pastor et al.**, 2023) (Figures **F9C, F10C**). Fe$_{PY}$, between 0.57% and 1.72% at Site U1552 (Figures **F9D, F10D**; Table **T6**), constitutes a major part of Fe$_{HR}$. However, Fe$_{HR}$ is less than half of the Fe$_T$ present in the samples analyzed (Figure **F8A**). Fe$_{HR}$/Fe$_T$ value is generally above 0.38 (Figure **F8B**) and indicates an enrichment in reactive iron in samples from Site U1552. The remaining fraction of Fe$_T$ is most likely contained in the poor-reactive silicates and unreactive iron minerals (Brocławik et al., 2020).

At Site U1552, with both holes considered (Holes U1552A and U1552C), AVS, detected in the samples, were not quantifiable. CRS values range 0.64%–2.1% with a peak of 2.1% at ~16.5 mbsf in Hole U1552A (Figure **F9D**) and with higher values in both holes in the gas hydrate zone (Figures **F9D, F10D**). CRS values are comparable to the TS contents measured on board (**Teske et al.**, 2021c) (Figure **F8C**) and suggest that pyrite dominates the mineral sulfur fraction. DOP values are between 0.78 and 0.96 (Figure **F8B**), with minimum values corresponding to peaks in Fe$_{ac}$, Fe$_{dith}$, and Fe$_{ox}$. High DOP values indicate a very efficient pyritization with most of Fe$_{HR}$ converted into pyrite (Figure **F8B**).

3.4. Influence of gas hydrates

The presence of gas hydrates between 25 and 45 mbsf at Site U1552 likely has an impact on the iron and sulfur minerals present in Guaymas Basin (Figure **F11**). A fraction of the methane migrates upward through the sediment and gets trapped and accumulated as methane hydrates. The higher flow of methane at Site U1552 may be supported by a decrease in pore water sulfate
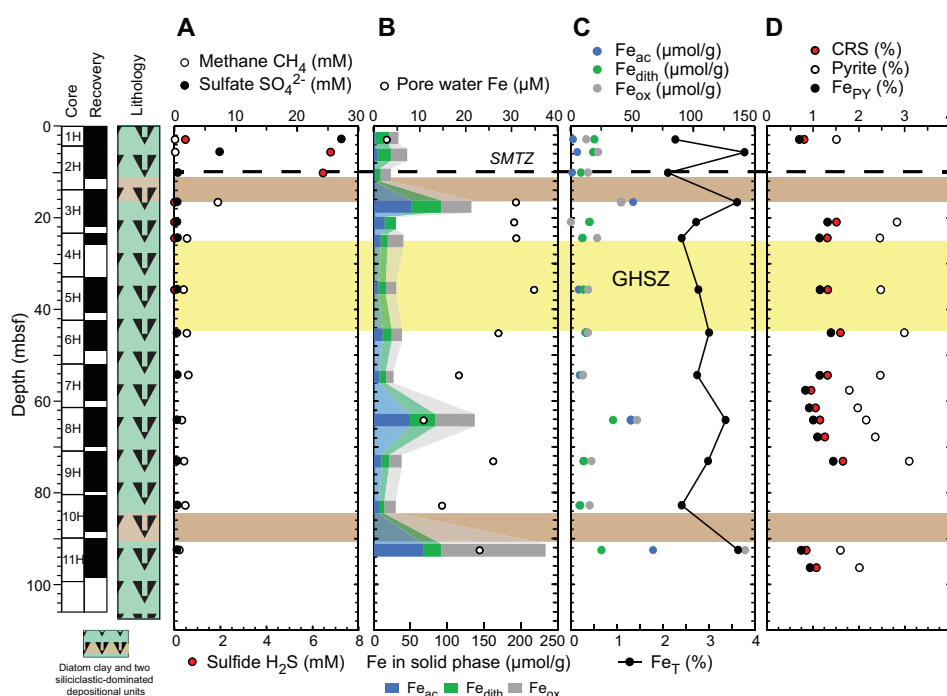

Figure F10. Downhole selected pore water properties and iron and sulfur speciation results, Hole U1552C. A. Pore water sulfate, dissolved sulfide, and methane concentrations. B. Dissolved iron (Fe^{2+}) in pore water and cumulative iron concentrations in solid phases extracted with acetate (Fe$_{ac}$), dithionite (Fe$_{dith}$), and oxalate (Fe$_{ox}$). C. Iron concentrations in solid phases extracted with acetate, dithionite, and oxalate, with total iron (Fe$_T$) (data from Pastor et al., 2023). D. Percentage concentrations of CRS, pyrite, and iron in form of pyrite. SMTZ at ~10 mbsf. Yellow = gas hydrate stability zone (GHSZ) (25–45 mbsf).

Table T6. Iron and sulfur speciation results, Site U1552. **Download table in CSV format.**

concentration at a faster rate at Site U1552 than at Site U1549 (Figures **F7A**, **F9A**, **F10A**). A higher flux of methane would also cause sulfate to react with methane in a narrower zone at Site U1552 compared to Site U1549, where the SMTZ seems to be broader and is 20 m deeper than at Site U1552 (Figure **F11**).

AOM reaction rate is likely increased and more intense at Site U1552 because of a higher methane flux there (Figure **F11A, F11E**). Other indexes point toward this assumption. Alkalinity, dissolved sulfide (ΣH_2S), and dissolved iron Fe(II) are higher in Site U1552 samples (Figure **F11F**). Variations in methane upward flow following possible gas hydrate dissociation events could be responsible for a dynamic state at Site U1552, where the SMTZ does not seem to be fixed over time because pyrite does not accumulate in the SMTZ compared to adjacent intervals.

The evolving SMTZ and gas hydrates at Site U1552 possibly explain the presence of the metastable authigenic iron sulfide, greigite, which has been identified at Site U1552. It is known that a close relationship exists between greigite authigenesis and gas hydrates with such occurrences reported in the Nankai Trough (e.g., Kars and Kodama, 2015a, 2015b; Shi et al., 2017), Cascadia margin
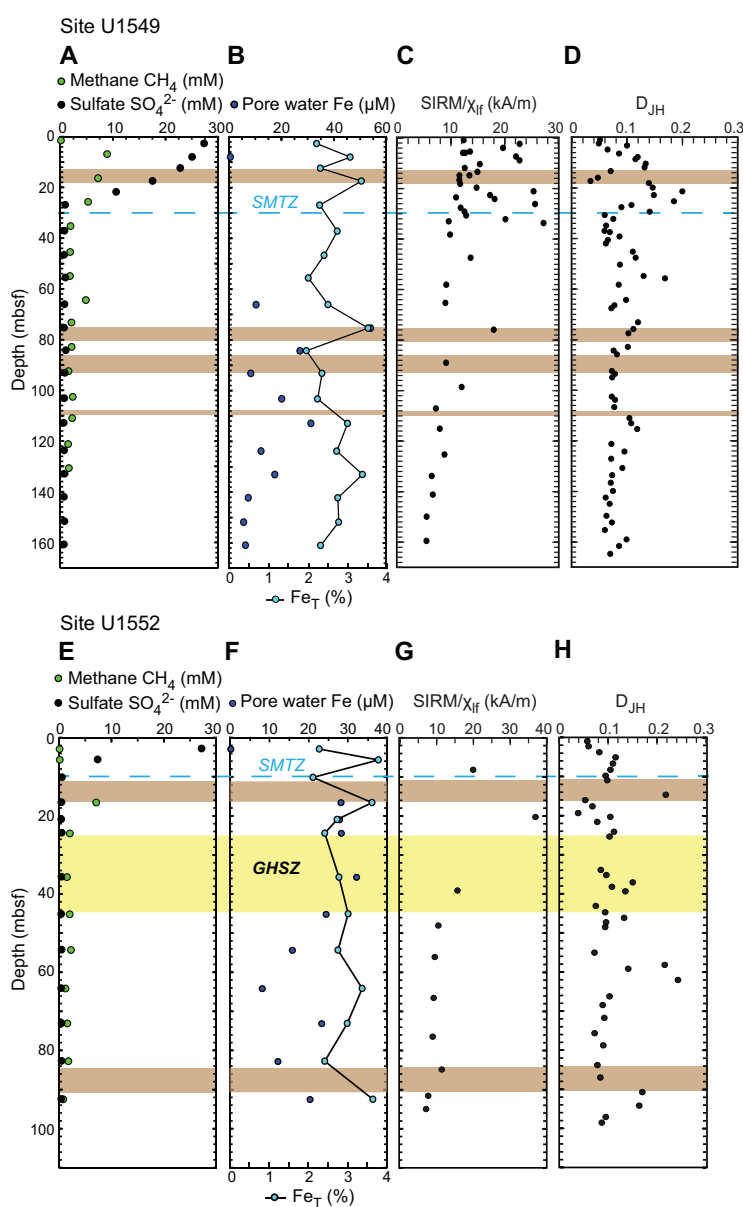

Figure F11. Selected key magnetic and geochemical properties. A–D. Site U1549. E–H. Site U1552.

(e.g., Larrasoaña et al., 2007; Housen and Musgrave, 1996) and Hikurangi margin (Kars et al., 2021a), for example. Greigite could be used as an indicator of intense AOM associated with gas hydrates. Authigenic greigite has an important impact on the paleomagnetic signal in marine sediments. The sediments recovered in Guaymas Basin were deposited during the normal Chron C1n and are too young to detect any secondary magnetization (**Teske et al.**, 2021a).

4. Acknowledgments

References

Alcott, L.J., Krause, A.J., Hammarlund, E.U., Bjerrum, C.J., Scholz, F., Xiong, Y., Hobson, A.J., Neve, L., Mills, B.J.W., März, C., Schnetger, B., Bekker, A., and Poulton, S.W., 2020. Development of iron speciation reference materials for palaeoredox analysis. Geostandards and Geoanalytical Research, 44(3):581–591. **https://doi.org/10.1111/ggr.12342**

Berner, R.A., 1981. A new geochemical classification of sedimentary environments. Journal of Sedimentary Research, 51(2):359–365. **https://doi.org/10.1306/212F7C7F-2B24-11D7-8648000102C1865D**

Bloemendal, J., King, J.W., Hall, F.R., and Doh, S.J., 1992. Rock magnetism of late Neogene and Pleistocene deep-sea sediments: relationship to sediment source, diagenetic processes, and sediment lithology. Journal of Geophysical Research: Solid Earth, 97(B4):4361–4375. **https://doi.org/10.1029/91JB03068**

Borowski, W.S., Paull, C.K., and Ussler, W., III, 1996. Marine pore-water sulfate profiles indicate in situ methane flux from underlying gas hydrate. Geology, 24(7):655–658. **https://doi.org/10.1130/0091-7613(1996)024<0655:MPWSPI>2.3.CO;2**

Brocławik, O., Łukawska-Matuszewska, K., Brodecka-Goluch, A., and Bolałek, J., 2020. Impact of methane occurrence on iron speciation in the sediments of the Gdansk Basin (Southern Baltic Sea). Science of The Total Environment, 721:137718. **https://doi.org/10.1016/j.scitotenv.2020.137718**

Canfield, D.E., Raiswell, R., Westrich, J.T., Reaves, C.M., and Berner, R.A., 1986. The use of chromium reduction in the analysis of reduced inorganic sulfur in sediments and shales. Chemical Geology, 54(1):149–155. **https://doi.org/10.1016/0009-2541(86)90078-1**

Carmody, R.W., Plummer, N., Busenberg, E., and Coplen, T.B., 1998. Methods for collection of dissolved sulfate and sulfide and analysis of their sulfur isotopic composition. USGS Open-File Report, 97-234. **https://doi.org/10.3133/ofr97234**

Dunlop, D.J., and Özdemir, Ö., 1997. Rock Magnetism: Fundamentals and Frontiers: Cambridge, United Kingdom (Cambridge University Press). **https://doi.org/10.1017/CBO9780511612794**

Froelich, P.N., Klinkhammer, G.P., Bender, M.L., Luedtke, N.A., Heath, G.R., Cullen, D., Dauphin, P., Hammond, D., Hartman, B., and Maynard, V., 1979. Early oxidation of organic matter in pelagic sediments of the eastern equatorial Atlantic: suboxic diagenesis. Geochimica et Cosmochimica Acta, 43(7):1075–1090. **https://doi.org/10.1016/0016-7037(79)90095-4**

Gott, C.S., 2016. Biogeochemical cycling in Costa Rica margin sediments as recorded in stable sulfur isotopes [MS thesis]. University of California, Riverside, CA. **https://escholarship.org/uc/item/8tz6498x**

Harrison, R.J., and Feinberg, J.M., 2008. FORCinel: an improved algorithm for calculating first-order reversal curve distributions using locally weighted regression smoothing. Geochemistry, Geophysics, Geosystems, 9(5). **https://doi.org/10.1029/2008GC001987**

Housen, B.A., and Musgrave, R.J., 1996. Rock-magnetic signature of gas hydrates in accretionary prism sediments. Seismic indications of gas hydrates in continental margins, 139(3):509–519. **https://doi.org/10.1016/0012-821X(95)00245-8**

Jørgensen, B.B., 1982. Mineralization of organic matter in the sea bed—the role of sulphate reduction. Nature, 296(5858):643–645. **https://doi.org/10.1038/296643a0**

Jørgensen, B.B., Beulig, F., Egger, M., Petro, C., Scholze, C., and Røy, H., 2019. Organoclastic sulfate reduction in the sulfate-methane transition of marine sediments. Geochimica et Cosmochimica Acta, 254:231-245. **https://doi.org/10.1016/j.gca.2019.03.016**

Jørgensen, B.B., and Kasten, S., 2006. Sulfur cycling and methane oxidation. In Schulz, H.D., and Zabel, M. (Eds.), Marine Geochemistry. Berlin (Springer), 271–309. **https://doi.org/10.1007/3-540-32144-6_8**

Karlin, R., 1990. Magnetite diagenesis in marine sediments from the Oregon continental margin. Journal of Geophysical Research: Solid Earth, 95(B4):4405–4419. **https://doi.org/10.1029/JB095iB04p04405**

Kars, M., Greve, A., and Zerbst, L., 2021a. Authigenic greigite as an indicator of methane diffusion in gas hydrate-bearing sediments of the Hikurangi margin, New Zealand. Frontiers in Earth Science, 9:603363. **https://doi.org/10.3389/feart.2021.603363**

Kars, M., and Kodama, K., 2015a. Authigenesis of magnetic minerals in gas hydrate-bearing sediments in the Nankai Trough, offshore Japan. Geochemistry, Geophysics, Geosystems, 16(3):947–961. **https://doi.org/10.1002/2014GC005614**

Kars, M., and Kodama, K., 2015b. Rock magnetic characterization of ferrimagnetic iron sulfides in gas hydrate-bearing marine sediments at Site C0008, Nankai Trough, Pacific Ocean, off-coast Japan. Earth, Planets and Space, 67(1):118. **https://doi.org/10.1186/s40623-015-0287-y**

Kars, M., Köster, M., Henkel, S., Stein, R., Schubotz, F., Zhao, X., Bowden, S.A., Roberts, A.P., and Kodama, K., 2021b. Influence of early low-temperature and later high-temperature diagenesis on magnetic mineral assemblages in marine sediments from the Nankai Trough. Geochemistry, Geophysics, Geosystems, 22(10):e2021GC010133. **https://doi.org/10.1029/2021GC010133**

Kashefi, K., and Lovley, D.R., 2003. Extending the upper temperature limit for life. Science, 301(5635):934. **https://doi.org/10.1126/science.1086823**

Knittel, K., and Boetius, A., 2009. Anaerobic oxidation of methane: progress with an unknown process. Annual Review of Microbiology, 63:311–334. **https://doi.org/10.1146/annurev.micro.61.080706.093130**

Köster, M., Kars, M., Schubotz, F., Tsang, M.-Y., Maisch, M., Kappler, A., Morono, Y., Inagaki, F., Heuer, V.B., Kasten, S., and Henkel, S., 2021. Evolution of (bio-)geochemical processes and diagenetic alteration of sediments along the tectonic migration of ocean floor in the Shikoku Basin off Japan. Geochemistry, Geophysics, Geosystems, 22(8):e2020GC009585. **https://doi.org/10.1029/2020GC009585**

Larrasoaña, J.C., Roberts, A.P., Musgrave, R.J., Gràcia, E., Piñero, E., Vega, M., and Martínez-Ruiz, F., 2007. Diagenetic formation of greigite and pyrrhotite in gas hydrate marine sedimentary systems. Earth and Planetary Science Letters, 261(3–4):350–366. **https://doi.org/10.1016/j.epsl.2007.06.032**

Lascu, I., Einsle, J.F., Ball, M.R., and Harrison, R.J., 2018. The vortex state in geologic materials: a micromagnetic perspective. Journal of Geophysical Research: Solid Earth, 123(9):7285–7304. **https://doi.org/10.1029/2018JB015909**

Leslie, B.W., Lund, S.P., and Hammond, D.E., 1990. Rock magnetic evidence for the dissolution and authigenic growth of magnetic minerals within anoxic marine sediments of the California continental borderland. Journal of Geophysical Research: Solid Earth, 95(B4):4437–4452. **https://doi.org/10.1029/JB095iB04p04437**

Lovley, D.R., 1991. Dissimilatory Fe(III) and Mn(IV) reduction. Microbiological Reviews, 55(2):259–287. **https://doi.org/10.1128/mr.55.2.259-287.1991**

Lu, R., and Banerjee, S.K., 1994. Magnetite dissolution in deep sediments and its hydrologic implication: a detailed study of sediments from site 808, leg 131. Journal of Geophysical Research: Solid Earth, 99(B5):9051–9059. **https://doi.org/10.1029/93JB03204**

Musgrave, R.J., Kars, M., and Vega, M.E., 2019. Progressive and punctuated magnetic mineral diagenesis: the rock magnetic record of multiple fluid inputs and progressive pyritization in a volcano-bounded basin, IODP Site U1437, Izu Rear Arc. Journal of Geophysical Research: Solid Earth, 124(6):5357–5378. **https://doi.org/10.1029/2018JB017277**

Muxworthy, A.R., and Dunlop, D.J., 2002. First-order reversal curve (FORC) diagrams for pseudo-single-domain magnetites at high temperature. Earth and Planetary Science Letters, 203(1):369–382. **https://doi.org/10.1016/S0012-821X(02)00880-4**

Muxworthy, A.R., and McClelland, E., 2000. Review of the low-temperature magnetic properties of magnetite from a rock magnetic perspective. Geophysical Journal International, 140(1):101–114. **https://doi.org/10.1046/j.1365-246x.2000.00999.x**

Özdemir, Ö., Dunlop, D.J., and Moskowitz, B.M., 2002. Changes in remanence, coercivity and domain state at low temperature in magnetite. Earth and Planetary Science Letters, 194(3):343–358. **https://doi.org/10.1016/S0012-821X(01)00562-3**

Passier, H.F., de Lange, G.J., and Dekkers, M.J., 2001. Magnetic properties and geochemistry of the active oxidation front and the youngest sapropel in the eastern Mediterranean Sea. Geophysical Journal International, 145(3):604–614. **https://doi.org/10.1046/j.0956-540x.2001.01394.x**

Passier, H.F., and Dekkers, M.J., 2002. Iron oxide formation in the active oxidation front above sapropel S1 in the eastern Mediterranean Sea as derived from low-temperature magnetism. Geophysical Journal International, 150(1):230–240. **https://doi.org/10.1046/j.1365-246X.2002.01704.x**

Pastor, L., Boissier, A., and Burin, C., 2023. Data report: wavelength dispersive X-ray fluorescence in sediments from all IODP Expedition 385 sites in the Guaymas Basin. In Teske, A., Lizarralde, D., Höfig, T.W., and the Expedition 385 Scientists, Guaymas Basin Tectonics and Biosphere. Proceedings of the International Ocean Discovery Program, 385: College Station, TX (International Ocean Discovery Program). **https://doi.org/10.14379/iodp.proc.385.203.2023**

Persad, L.D., and Marsaglia, K.M., 2023. Data report: detailed lithologic columns for IODP Expedition 385 and DSDP Leg 64 sites in the Guaymas Basin, Gulf of California, Mexico. In Teske, A., Lizarralde, D., Höfig, T.W., and the

Expedition 385 Scientists, Guaymas Basin Tectonics and Biosphere. Proceedings of the International Ocean Discovery Program, 385: College Station, TX (International Ocean Discovery Program). **https://doi.org/10.14379/iodp.proc.385.202.2023**

Pike, C.R., Roberts, A.P., and Verosub, K.L., 1999. Characterizing interactions in fine magnetic particle systems using first order reversal curves. Journal of Applied Physics, 85(9):6660–6667. **https://doi.org/10.1063/1.370176**

Poulton, S.W., and Canfield, D.E., 2005. Development of a sequential extraction procedure for iron: implications for iron partitioning in continentally derived particulates. Chemical Geology, 214(3):209–221. **https://doi.org/10.1016/j.chemgeo.2004.09.003**

Poulton, S.W., and Raiswell, R., 2002. The low-temperature geochemical cycle of iron: from continental fluxes to marine sediment deposition. American Journal of Science, 302(9). **https://doi.org/10.2475/ajs.302.9.774**

Raiswell, R., and Canfield, D.E., 2012. The iron biogeochemical cycle past and present. Geochemical Perspectives, 1(1). **https://doi.org/10.7185/geochempersp.1.1**

Roberts, A.P., 2015. Magnetic mineral diagenesis. Earth-Science Reviews, 151:1–47. **https://doi.org/10.1016/j.earscirev.2015.09.010**

Roberts, A.P., Almeida, T.P., Church, N.S., Harrison, R.J., Heslop, D., Li, Y., Li, J., Muxworthy, A.R., Williams, W., and Zhao, X., 2017. Resolving the origin of pseudo-single domain magnetic behavior. Journal of Geophysical Research: Solid Earth, 122(12):9534–9558. **https://doi.org/10.1002/2017JB014860**

Roberts, A.P., Chang, L., Rowan, C.J., Horng, C.-S., and Florindo, F., 2011. Magnetic properties of sedimentary greigite (Fe_3S_4): an update. Reviews of Geophysics, 49(1):RG1002. **https://doi.org/10.1029/2010RG000336**

Roberts, A.P., Liu, Q., Rowan, C.J., Chang, L., Carvallo, C., Torrent, J., and Horng, C.-S., 2006. Characterization of hematite (α-Fe_2O_3), goethite (α-FeOOH), greigite (Fe_3S_4), and pyrrhotite (Fe_7S_8) using first-order reversal curve diagrams. Journal of Geophysical Research: Solid Earth, 111(B12). **https://doi.org/10.1029/2006JB004715**

Roberts, A.P., Pike, C.R., and Verosub, K.L., 2000. First-order reversal curve diagrams: a new tool for characterizing the magnetic properties of natural samples. Journal of Geophysical Research: Solid Earth, 105(B12):28461–28475. **https://doi.org/10.1029/2000JB900326**

Roberts, A.P., Tauxe, L., Heslop, D., Zhao, X., and Jiang, Z., 2018. A critical appraisal of the "Day" diagram. Journal of Geophysical Research: Solid Earth, 123(4):2618–2644. **https://doi.org/10.1002/2017JB015247**

Shi, M., Wu, H., Roberts, A.P., Zhang, S., Zhao, X., Li, H., Su, X., Yang, T., Chang, L., Hu, P., Zhao, X., and Wang, H., 2017. Tectonic, climatic, and diagenetic control of magnetic properties of sediments from Kumano Basin, Nankai margin, southwestern Japan. Marine Geology, 391:1–12. **https://doi.org/10.1016/j.margeo.2017.07.006**

Teske, A., Lizarralde, D., and Höfig, T.W., 2018. Expedition 385 Scientific Prospectus: Guaymas Basin Tectonics and Biosphere. International Ocean Discovery Program. **https://doi.org/10.14379/iodp.sp.385.2018**

Teske, A., Lizarralde, D., Höfig, T.W., Aiello, I.W., Ash, J.L., Bojanova, D.P., Buatier, M.D., Edgcomb, V.P., Galerne, C.Y., Gontharet, S., Heuer, V.B., Jiang, S., Kars, M.A.C., Khogenkumar Singh, S., Kim, J.-H., Koornneef, L.M.T., Marsaglia, K.M., Meyer, N.R., Morono, Y., Negrete-Aranda, R., Neumann, F., Pastor, L.C., Peña-Salinas, M.E., Pérez Cruz, L.L., Ran, L., Riboulleau, A., Sarao, J.A., Schubert, F., Stock, J.M., Toffin, L.M.A.A., Xie, W., Yamanaka, T., and Zhuang, G., 2021a. Expedition 385 summary. In Teske, A., Lizarralde, D., Höfig, T.W., and the Expedition 385 Scientists, Guaymas Basin Tectonics and Biosphere. Proceedings of the International Ocean Discovery Program, 385: College Station, TX (International Ocean Discovery Program). **https://doi.org/10.14379/iodp.proc.385.101.2021**

Teske, A., Lizarralde, D., Höfig, T.W., Aiello, I.W., Ash, J.L., Bojanova, D.P., Buatier, M.D., Edgcomb, V.P., Galerne, C.Y., Gontharet, S., Heuer, V.B., Jiang, S., Kars, M.A.C., Khogenkumar Singh, S., Kim, J.-H., Koornneef, L.M.T., Marsaglia, K.M., Meyer, N.R., Morono, Y., Negrete-Aranda, R., Neumann, F., Pastor, L.C., Peña-Salinas, M.E., Pérez Cruz, L.L., Ran, L., Riboulleau, A., Sarao, J.A., Schubert, F., Stock, J.M., Toffin, L.M.A.A., Xie, W., Yamanaka, T., and Zhuang, G., 2021b. Site U1549. In Teske, A., Lizarralde, D., Höfig, T.W., and the Expedition 385 Scientists, Guaymas Basin Tectonics and Biosphere. Proceedings of the International Ocean Discovery Program, 385: College Station, TX (International Ocean Discovery Program). **https://doi.org/10.14379/iodp.proc.385.106.2021**

Teske, A., Lizarralde, D., Höfig, T.W., Aiello, I.W., Ash, J.L., Bojanova, D.P., Buatier, M.D., Edgcomb, V.P., Galerne, C.Y., Gontharet, S., Heuer, V.B., Jiang, S., Kars, M.A.C., Khogenkumar Singh, S., Kim, J.-H., Koornneef, L.M.T., Marsaglia, K.M., Meyer, N.R., Morono, Y., Negrete-Aranda, R., Neumann, F., Pastor, L.C., Peña-Salinas, M.E., Pérez Cruz, L.L., Ran, L., Riboulleau, A., Sarao, J.A., Schubert, F., Stock, J.M., Toffin, L.M.A.A., Xie, W., Yamanaka, T., and Zhuang, G., 2021c. Site U1552. In Teske, A., Lizarralde, D., Höfig, T.W., and the Expedition 385 Scientists, Guaymas Basin Tectonics and Biosphere. Proceedings of the International Ocean Discovery Program, 385: College Station, TX (International Ocean Discovery Program). **https://doi.org/10.14379/iodp.proc.385.109.2021**

Teske, A., Wegener, G., Chanton, J.P., White, D., MacGregor, B., Hoer, D., de Beer, D., Zhuang, G., Saxton, M.A., Joye, S.B., Lizarralde, D., Soule, S.A., and Ruff, S.E., 2021d. Microbial communities under distinct thermal and geochemical regimes in axial and off-axis sediments of Guaymas Basin. Frontiers in Microbiology, 12:633649. **https://doi.org/10.3389/fmicb.2021.633649**

Treude, T., Niggemann, J., Kallmeyer, J., Wintersteller, P., Schubert, C.J., Boetius, A., and Jørgensen, B.B., 2005. Anaerobic oxidation of methane and sulfate reduction along the Chilean continental margin. Geochimica et Cosmochimica Acta, 69(11):2767–2779. **https://doi.org/10.1016/j.gca.2005.01.002**

van Baak, C.G.C., Vasiliev, I., Palcu, D.V., Dekkers, M.J., and Krijgsman, W., 2016. A greigite-based magnetostratigraphic time frame for the Late Miocene to Recent DSDP Leg 42B Cores from the Black Sea. Frontiers in Earth Science, 4. **https://doi.org/10.3389/feart.2016.00060**

van Velzen, A.J., and Zijderveld, J.D.A., 1992. A method to study alterations of magnetic minerals during thermal demagnetization applied to a fine-grained marine marl (Trubi formation, Sicily). Geophysical Journal International, 110(1):79–90. **https://doi.org/10.1111/j.1365-246X.1992.tb00715.x**

Vargas, M., Kashefi, K., Blunt-Harris, E.L., and Lovley, D.R., 1998. Microbiological evidence for Fe(III) reduction on early Earth. Nature, 395(6697):65–67. **https://doi.org/10.1038/25720**

Willie, S., Nadeau, K., Pihillagawa Gedara, I., Yang, L., Clancy, V., Grinberg, P., Kumkrong, P., Mercier, P.H.J., Mihai, O., Tyo, D.D., Jiang, C., Kingston, D.M., Meija, J., Maxwell, P., and Mester, Z., 2014. MESS-4: marine sediment certified reference material for total and extractable metal content. **https://doi.org/10.4224/crm.2014.mess-4**